

Time-dependent CO depletion during the formation of protoplanetary disks

C. Brinch, R. J. van Weeren, and M. R. Hogerheijde

Leiden Observatory, Leiden University, P.O. Box 9513, 2300 RA Leiden, The Netherlands
e-mail: brinch@strw.leidenuniv.nl

ABSTRACT

Context. Understanding the gas abundance distribution is essential when tracing star formation using molecular line observations. Changing density and temperature conditions cause gas to freeze-out onto dust grains, and this needs to be taken into account when modeling a collapsing molecular cloud.

Aims. This study aims to provide a realistic estimate of the CO abundance distribution throughout the collapse of a molecular cloud. We provide abundance profiles and synthetic spectral lines which can be compared to observations.

Methods. We use a 2D hydrodynamical simulation of a collapsing cloud and subsequent formation of a protoplanetary disk as input for the chemical calculations. From the resulting abundances, synthetic spectra are calculated using a molecular excitation and radiation transfer code.

Results. We compare three different methods to calculate the abundance of CO. Our models also consider cosmic ray desorption and the effects of an increased CO binding energy. The resulting abundance profiles are compared to observations from the literature and are found to agree well.

Conclusions. The resulting abundance profiles agree well with analytic approximations, and the corresponding line fluxes match observational data. Our developed method to calculate abundances in hydrodynamical simulations should greatly aid in comparing these to observations, and can easily be generalized to include gas-phase reaction networks.

Key words. Astrochemistry – Hydrodynamics – Stars: formation – ISM: molecules – ISM: clouds

1. Introduction

The study of low-mass Young Stellar Objects (YSOs), from early protostellar cores to T Tauri stars surrounded by disks, involves observations of either the thermal emission from dust grains or molecular line emission. While dust emission yields information about the temperature profile (e.g., Draine & Lee 1984), and, through measurements of the shape of the Spectral Energy Distribution, the evolutionary stage (Lada & Wilking 1984; Adams et al. 1987), spectral lines are the only way to constrain the kinematical properties of YSOs. The interpretation of molecular lines are crucial for the understanding of protoplanetary disk formation and the distribution of angular momentum during these stages of star formation (Evans 1999). However, deriving the gas motion from spectral line profiles is complicated by degeneracies between the velocity field topology, inclination of the angular momentum axis, optical depth, and geometrical effects (Brinch et al. 2007).

In addition to these effects, molecular abundances may vary greatly. The gas abundance is determined by the ongoing chemistry driven by the co-evolving density and temperature distributions, and to some extent also the velocity field. The variation in molecular abundances throughout a YSO may have a huge impact on line profiles and therefore it is important to understand the chemistry in order to interpret these line profiles. The effect of the chemistry is enhanced when observations at higher resolution are done. If the observations are done at a relatively low resolution ($\gtrsim 10''$), the emission is smeared out over a large portion of the object and therefore an average constant abundance is mostly adequate. However, when going to a higher resolution, using sub-millimeter interferometry ($\sim 1''$), the emission is aver-

aged over a smaller part of the object and thus variations in the abundance need to be taken into account.

The problem of determining the abundance distribution has been addressed before in the literature. Lee et al. (2004) took a semi-analytical approach using a self-similar collapse of an isothermal sphere in which they followed “fluid-elements”. In that paper, the chemistry was followed in a series of Bonnor-Ebert spheres during the pre-stellar phase and in a self-similar inside-out collapse during the protostellar phase. This model provides a good analytical description of the early stages of star formation, but, lacking any rotational velocity, no disk is formed in this scenario. Aikawa et al. (2001, 2003, 2005) followed the chemical evolution of contracting pre-stellar clouds using an approach similar to Lee et al. (2004) but using an isothermal cloud collapse only. Their calculations consider only the very early stages of the star formation process. Jørgensen et al. (2002, 2005) introduced the “drop model”, where chemical depletion occurs as a step function when certain temperature and density conditions of any underlying model are met. While this approach is simple yet quite successful, there may be cases where the abundance changes only very gradually so that a step function is no longer a good approximation. More recently, Tsamis et al. (2008) calculated HCO^+ , CS, and N_2H^+ abundances and spectra from a simulation of an inside-out collapsing core.

In this paper we investigate detailed evolution of the gas-phase and solid state abundance of CO in a collapsing, rotating core. We base our study on a hydrodynamical simulation, where we follow the CO freeze-out and evaporation for a number of test particles that flow with the gas. The lay-out of the paper is as follows: In Section 2 we present our numerical simulations

and the equations used to solve the CO freeze-out chemistry. In Section 3 we show three different chemical models and how our results compare to observations as well as the results of previous papers. Sections 4 and 5 hold a discussion and a summary respectively.

2. Tracing chemistry during disk formation

2.1. The physical model

Instead of using an analytic description of the gravitational collapse and subsequent disk formation, we use a grid-based 2D axis-symmetric hydrodynamical scheme. The code which is used is described in Yorke & Bodenheimer (1999) and in particular we adopt the J-type model described in that paper.

The initial conditions for this model are a $1 M_{\odot}$ isothermal sphere with a temperature of 10 K and a power-law density slope of $\rho \propto r^{-2}$. The cloud has an outer radius of 1×10^{15} m (6667 AU), and an initial solid-body rotational perturbation of $1 \times 10^{-13} \text{ s}^{-1}$ is given. The model evolves under the action of gravity while the temperature is solved for self-consistently using an approximate radiation transfer method. Angular momentum is transferred through artificial viscosity using an α -prescription (Shakura & Sunyaev 1973).

The age of the simulated system is described in terms of the initial free-fall timescale,

$$t_{ff} = \sqrt{\frac{\pi^2 R^3}{8GM}}, \quad (1)$$

where M is the mass of the cloud and R is the radius. For the initial conditions in our particular simulation one free-fall time is 1×10^5 yr. We let the simulation run for about $2.6 t_{ff}$ at which point the simulation terminates due to extreme velocities near the center. Figure 1 shows four time snapshots at characteristic ages. We use the same four snapshots throughout this paper, at times of 0.0, 0.5, 1.5, and 2.5 t_{ff} (with the exception of Fig. 1, where we use a few snapshots later than $t = 0.0$ in order for the temperature to have evolved slightly from the isothermal initial condition).

The luminosity is given by the sum of the intrinsic stellar luminosity and the accretion luminosity

$$L_{acc} = \frac{3}{4} \frac{GM_* \dot{M}}{R_*}, \quad (2)$$

where M_* is the mass of the star, R_* the radius of the star, and \dot{M} the mass flux onto the star. The total luminosity is shown, plotted as a function of free-fall time, in Fig. 2. After the initial increase in the luminosity, it drops for a while, after which it steeply increases again and then slowly falls off linearly for the remainder of the simulation. As described in Yorke & Bodenheimer (1999), the smooth increase and the drop around $0.5 t_{ff}$ is dominated by the accretion luminosity where low angular momentum material is able to fall directly onto the star. The sharp increase in luminosity marks the formation of an equilibrium disk and from then on, the intrinsic stellar luminosity dominates the total luminosity.

The hydrodynamical simulations does not include any chemistry and because of that, we cannot let the state of the molecules, whether they are in the gas phase or locked in an ice matrix, couple back to the hydrodynamics. We therefore determine the abundance by post-processing the result of the hydrodynamical calculations. We follow the chemistry by populating the computational domain of the first snapshot with trace particles. These

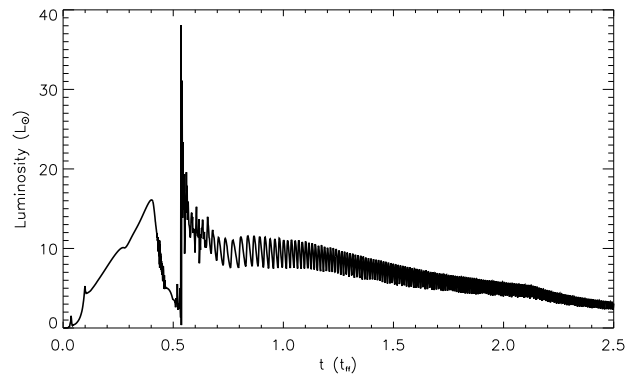


Fig. 2. The time evolution of the luminosity of the central source in the hydrodynamical simulation. This figure compares to Fig. 7 in Yorke & Bodenheimer (1999).

particles are massless and do not interact with each other in any way. The trace particles are positioned evenly in the radial direction and 9×10^5 particles are used. Every trace particle represents the local molecular environment and carries information on the state of the molecules (ice or gas). The particles are then allowed to follow the flow, predetermined by the hydrodynamical calculations, and the state of the particles is updated as temperature and density conditions change throughout the hydrodynamical simulation. Finally, the state of the trace particles are mapped back onto the hydro-grid at each output time step, so that a complete history from $t=0.0 t_{ff}$ to $t=2.5 t_{ff}$ of the CO abundance as function of R and z is linked to the density and temperature. Taking the CO distribution into account, we can use each of these time snapshots as input models for our 2D line excitation and radiative transfer code *RATRAN* (Hogerheijde & van der Tak 2000) to predict line profiles of CO and its optically thin isotopologue $C^{18}O$.

Before proceeding with the freeze-out calculations, it is interesting to consider the dynamics of the trace particles in order to develop an understanding of the environments that the particles traverse. By a simple radial color coding of the particles, we can effectively visualize the flow within the hydrodynamical simulation and track how material is accreted onto the disk. Four snapshots of the particle distribution are shown in Fig. 3 where the shading of the particles refers to their initial distance from the center. The disk is seen to be layered vertically rather than radially which is somewhat counterintuitive. The vertical layering arises because material joins the disk from above. As the disk spreads viscously due to conservation of angular momentum, a shock front propagates outwards, pushing aside infalling material. The only possible path of the particles is therefore upwards and over the disk lobe until they can rain down onto the disk at smaller radii. This rolling motion, is also reflected in the strong vertical mixing in the outer disk. However, this behavior may be an artifact related to the 2D nature of the hydrodynamical code. In a 3D simulation, particles would also be able to dissipate in the azimuthal direction, which would likely change their motions.

2.2. Freeze-out and evaporation

In general, molecular gas abundances depend on reaction rates and phase transitions. However, under the physical conditions present in our model, only the latter has any significant impact on the CO abundance. The state of CO is governed by rate equa-

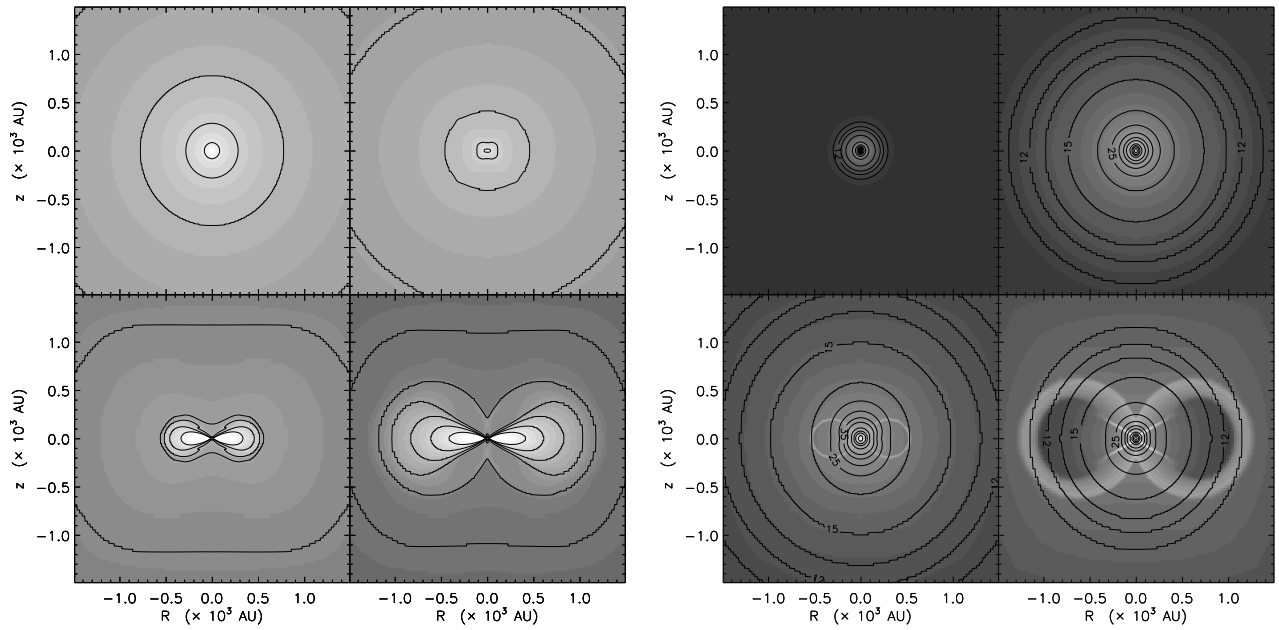


Fig. 1. The density (left panel) and temperature (right panel) contours of four time snapshots of the hydrodynamical simulation. Time progresses from left to right, top to bottom at $t = \{0.0(6), 0.5, 1.5, 2.5\} t_{ff}$. In the right panel, contour lines refer to the dust temperature, while the color scale denote the gas temperature.

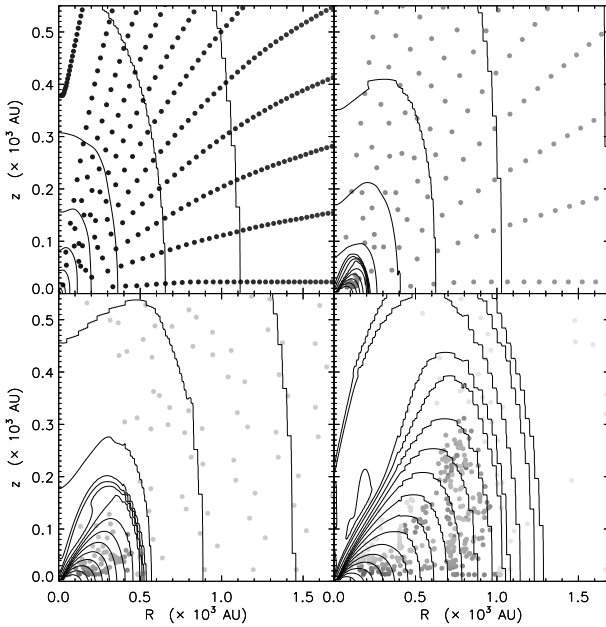


Fig. 3. Trace particle motion in the hydrodynamical simulation. The particles are color coded according to their initial radial position. Contour lines describe the density. The vertical color bar shows the particles initial distance from the center. The four panels (from the top-left to bottom-right) show the particle positions at $t=0.0, 0.5, 1.5$, and $2.5 t_{ff}$.

tions. The two main mechanisms are depletion, where gas phase molecules freeze-out onto grains, and desorption, where solid state molecules evaporate into the gas phase.

The depletion rate λ used in this paper is given by the equation (e.g., Charnley et al. 2001),

$$\lambda = \pi a^2 \sqrt{\frac{8kT_g}{\pi m_{CO}}} n_{grain}, \quad (3)$$

where T_g is the gas temperature, m_{CO} is the mass of a CO molecule, and n_{grain} is the grain number density, assuming a grain abundance of 1.33×10^{-12} relative to the hydrogen nucleon density. For the mean grain size a we adopt the value of $0.1 \mu\text{m}$. We also assume a sticking probability of unity.

A similar equation can be written for the desorption of molecules. The thermal desorption rate is given by Watson & Salpeter (1972),

$$\xi_{th} = \nu(X) e^{\left(\frac{-E_b(X)}{k_b T_d}\right)}, \quad (4)$$

where k_b is Boltzmann's constant, T_d is the dust temperature, $\nu(X)$ is the vibrational frequency of X in its binding site (Hasegawa et al. 1992), and $E_b(X)$ is the binding energy of species X onto the dust grain. In this paper we use a default binding energy of 960 K, but other values, corresponding to mantles which are not composed of pure CO ice, are explored as well in Sect. 3.4.

A second desorption mechanism which is taken into account is cosmic ray induced desorption. This mechanism was first proposed by Watson & Salpeter (1972). Energetic nuclei might eject molecules from grain surfaces by either raising the temperature of the entire grain or by spot heating near the impact site. The formulation of Hasegawa & Herbst (1993) is used to calculate the cosmic ray desorption rate,

$$\xi_{cr} = 3.16 \times 10^{-19} \xi_{th} \Big|_{T_d=70K}. \quad (5)$$

Cosmic ray desorption can be added to the thermal desorption, effectively preventing a depletion of 100% under any condition.

With the depletion and desorption rates, defining f_d to be the normalized fractional depletion, we can write an equation for f_d ,

$$\frac{df_d(\mathbf{r}, t)}{dt} = \lambda(\mathbf{r}, t)f_d(\mathbf{r}, t) - \xi(\mathbf{r}, t)(1 - f_d(\mathbf{r}, t)), \quad (6)$$

in which we implicitly use the boundary condition that the sum of CO molecules in solid state and in the gas phase is constant.

Equation 6 is a very general one and the rate functions can easily be changed so that the equation describes other reactions. van Weeren (2007) shows that in principle a whole set of such equations can be solved simultaneously using gas phase reaction rates from e.g., the UMIST database (Woodall et al. 2007) although computational demand becomes an issue for a full network.

3. Results

To obtain abundance distributions we evaluate Eq. 6 using the gas temperature T_g , the dust temperature T_d , and the mass density (we assume that H_2 is the main mass reservoir and that the gas-to-dust ratio is 100:1) from the hydrodynamical simulation. We assume that the cloud has been in hydrostatic equilibrium prior to collapse for 3×10^5 yr ($=1 \times 10^{13}$ s). The density profile before collapse is given by a spherical power-law with a uniform temperature as described in Sect. 2. Starting with a pure gas phase abundance of 2×10^{-4} molecules relative to H_2 , we let the abundance evolve for 3×10^5 yr with a constant temperature of 10 K and a static density profile. The new CO abundance serves as initial condition for the collapse, i.e., the start of the hydrodynamical simulation which defines $t = 0$. In the following we present three different ways to obtain the abundance profiles.

3.1. Model 1: Drop abundance

This approach is denoted the drop abundance model, because it follows directly from the method presented by Jørgensen et al. (2005). In this approach we do not actually solve Eq. 6, but rather consider the rate equations 3 and 4. The rate equations are inverted to obtain a characteristic time scale, and at any given time in the simulation, this time scale is evaluated based on the current density and temperature conditions. If the freeze-out time scale is shorter than the evaporation time scale, the gas phase abundance drops to a preset level (sufficiently low, i.e., several orders of magnitude) but if the actual age of the cloud is shorter than the freeze-out time scale, the gas phase abundance is kept at its initial value. Using this approach, the resulting profile is a step function where all CO is either in the gas phase or in the solid state. The movement of the trace particles does not affect the result since the abundance is determined only from the current local conditions. The effect of cosmic ray desorption is implicitly accounted for by not letting the abundance drop to zero, but only two or three orders of magnitude, although freeze-out conditions are met.

The result is shown in Fig. 4. The top panel shows the radial abundance profile along the disk mid-plane ($z=0$), while the lower panel shows the two dimensional distribution. The result of this drop abundance approach supports the idea of an evolution of the CO abundances from a pre-stellar core to a Class I object, proposed by Jørgensen et al. (2005). The maximum size of our depleted zone is ~ 6000 AU, just before the collapse sets in, and shrinks to ~ 500 AU (when averaged in radial and polar directions) as the cloud collapses and the disk is formed. The inner evaporated zone has a radius of ~ 1000 AU, in agreement with values derived in Jørgensen et al. (2005).

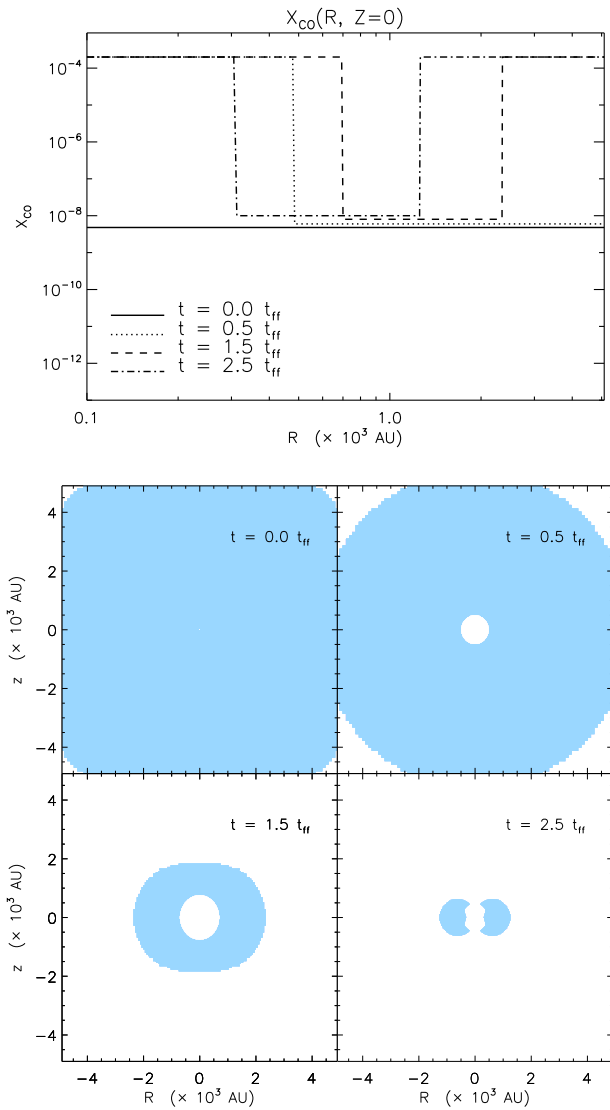


Fig. 4. This figure shows the abundance distribution of Model 1. The top panel shows the radial abundance profile through the mid-plane of the disk. The bottom panel shows the spatial abundance distribution. The shaded area is where molecules are frozen out. The unit on the y-axis of the top panel is fractional abundance.

3.2. Model 2: Variable freeze-out

The second method is similar to Model 1 except that instead of using the time scales, we use the actual rate equations which allows the trace particles to be in a mixed state. The values for λ and ξ are calculated for all \mathbf{r} using the current $n(\mathbf{r})$ and $T(\mathbf{r})$ and Eq. 6 is solved to obtain the fraction of gas phase CO to solid state CO for each trace particle position. In this model, we still do not consider the history of the trace particles and thus the motion of the particles is irrelevant and the time dependence of ξ and λ in Eq. 6 drops out. Plots of the abundance distributions are shown in Fig. 5. The profiles of Model 2 are quite similar to the ones from Model 1, except for the gradual change from pure gas phase to pure solid state. Especially the inner edge is well approximated by the step function of Model 1 because of the exponential factor in the evaporation, described by Eq. 4. The main difference between the two models is the outer edge, and especially at earlier times, where the gradient is more shallow.

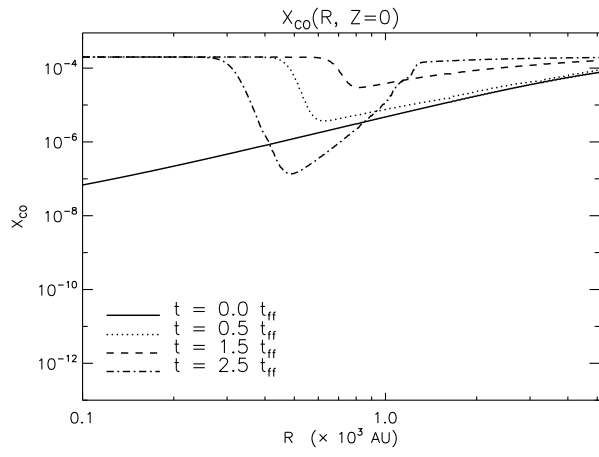


Fig. 5. Abundance distribution of Model 2. Otherwise identical to 4.

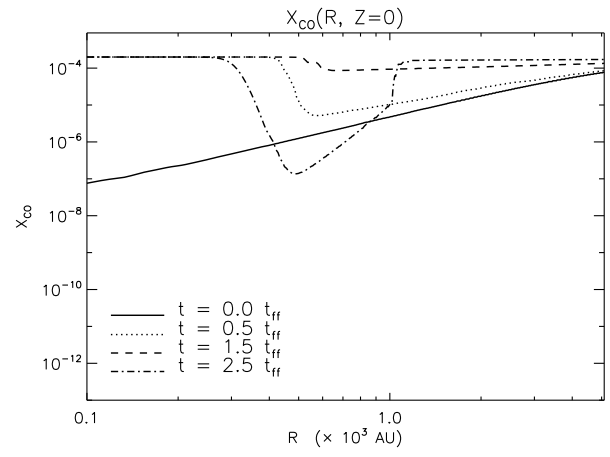


Fig. 6. Abundance distribution of Model 3. Otherwise similar to 4.

3.3. Model 3: Dynamical evolution

Our final model takes the motion of the trace particles and their chemical history into account. Freeze-out and evaporation rates are calculated dynamically for each time step and composition of the particles is used as initial condition for Eq. 6. For example, the depletion in a certain area represented by a trace particle depends on where this particle has come from, which we know, because the trace particles follow the flow calculated in the hydrodynamical simulation. Two trace particles may pass by the same region at the same time and experience the same desorption and depletion conditions. However, they may have come from different areas, e.g., one may have spent time in a warmer region and the other may come from a colder region and therefore they will leave the place with different compositions.

Figure 6 shows the abundance distributions for this model. Surprisingly, the profiles are not very different from those of Model 2. A difference only occurs when the dynamical time scale is comparable to the chemical time scale. In this case, a gas phase trace particle may move out of a depletion zone faster than depletion can make any significant change to its composition, or vice versa. The evaporation front around the disk is also sharper

compared to Model 2 which makes Model 3 appear almost like a step function in the latter part of the simulation.

3.4. Cosmic ray desorption and increased binding energy

We now investigate the effects of excluding the cosmic ray desorption term (Eq. 5) to see what effect this mechanism has on the abundances. We also increase the CO binding energy E_b in Eq. 4 in order to emulate different ice mantle compositions. In the following we use Model 3 as a template.

Cosmic ray desorption ensures that depletion can never reach 100% as long as cosmic rays are able to penetrate the cloud and remove molecules from the ice matrix. If no other desorption mechanisms were present, dark cold molecular clouds would have a very high degree of depletion since thermal desorption is largely ineffective at low temperatures. However, Caselli et al. (1999) find no evidence for such high depletion factors and therefore some other desorption mechanism (such as for instance cosmic ray desorption) must play a certain role in these environments. However, to see exactly how much evaporation cosmic rays account for, we have calculated Model 3 without the cosmic ray desorption term. Figure 7 shows these abundance dis-

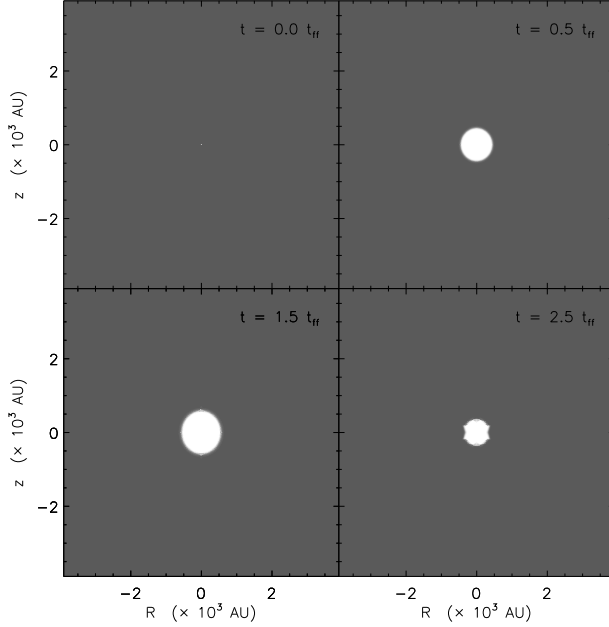
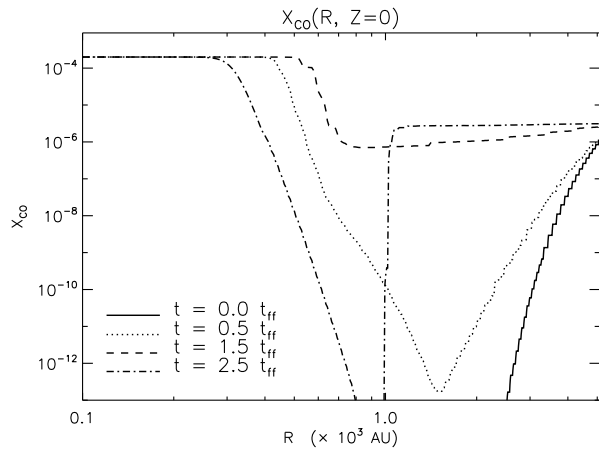


Fig. 7. Abundance distribution of Model 3 without cosmic ray desorption and the default binding energy of 960 K. Otherwise similar to 4.

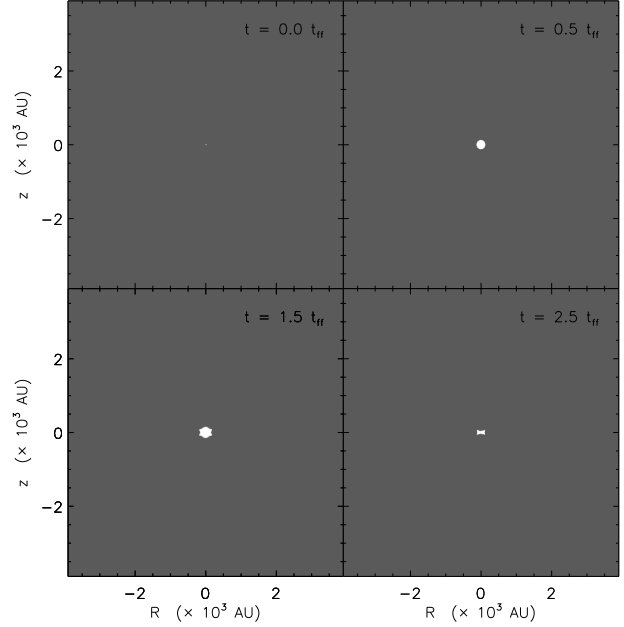
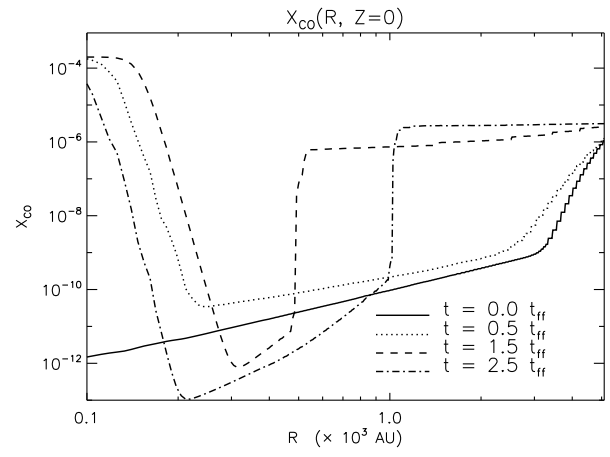


Fig. 8. Abundance distribution of Model 3, including cosmic rays, but with a CO binding energy of 1740 K. Otherwise similar to 4.

tributions. The profiles are largely similar to Model 3, but the amount of depletion is, as expected, about three orders of magnitude higher.

Including cosmic ray desorption obviously has a big impact on the amount of gas phase molecules in the cloud, raising the gas-phase abundance significantly. However the effect of cosmic ray desorption can be countered by a larger binding energy between molecule and grain surface. For example, raising the binding energy from 960 K to 1740 K almost entirely compensates the effect of cosmic ray desorption, when the depletion is averaged over the entire model.

An increased binding energy applies when the CO ice mantle is mixed with other species, typically water ice or NH_3 ice (Fraser et al. 2004). Another way to obtain a spread in binding energies is when the ice surfaces are not even, e.g., differently layered ices, varying mantle thickness, rough surfaces, etc. If the grains are more fractal, with cavities which can trap CO molecules, it will become harder to desorb these molecules, effectively raising the binding energy. Laboratory experiments of Collings et al. (2004) even showed multiple peaks in the CO desorption spectrum, implying a range of binding energies. In

Fig. 8 it can be seen that the inner most evaporation zone is consistently and significantly smaller when the binding energy is increased compared to when cosmic rays are omitted, suggesting that the two effects can be disentangled by high-resolution observations.

3.5. Comparison to observations

We compare our results with observations of CO abundances and depletion factors. The fractional depletion f_d of CO for the various models are shown in Fig. 9. The highest depletion factors occur at the end of the pre-stellar core phase just before collapse. Observations show that depletion factors decrease with decreasing envelope mass (Jørgensen et al. 2002). We indeed see the depletion decrease after the core begins to collapse due to CO evaporation close to the protostar. At the same time the envelope density decreases which also lowers the global fractional depletion, defined as the ratio of the total number of gas phase CO molecules to H_2 molecules in the entire model.

Freeze-out in the disk is most pronounced for Model 3 including cosmic ray desorption and a high CO binding energy.

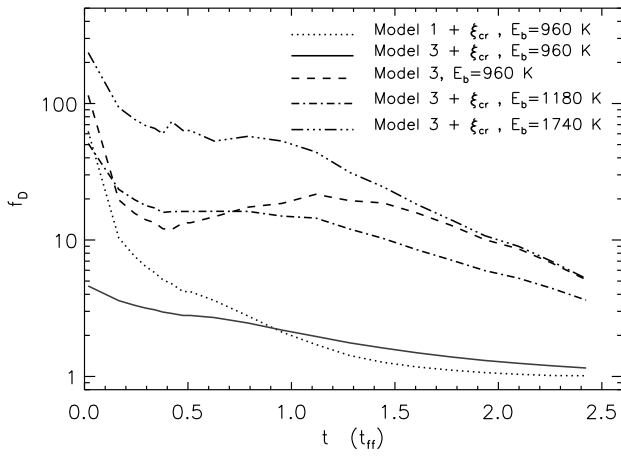


Fig. 9. The global fractional depletion in the various models. The small bump in the curves around $0.5 t_{ff}$ is due to a change in the luminosity output of the central source as the disk is formed.

The same model, but with a binding energy of 960 K, gives a very low depletion factor at the start of the collapse. Although low values of f_d have been measured (e.g., Bacmann et al. 2002), most observations point toward a higher value, $f_d \geq 10$, in pre-stellar cores (e.g., Crapsi et al. 2004; Bergin et al. 2002; Jessop & Ward-Thompson 2001). The low value of f_d we find means that either the binding energy is larger than 960 K or that we overestimate the cosmic ray desorption rate. Indeed, Shen et al. (2004) showed that the importance of cosmic ray heating has been overestimated by previous authors. A third possibility is that CO can be converted into other species, resulting in a lower abundance, but since we only model CO we cannot quantify this effect.

As mentioned above, a correlation has been found between the amount of depletion and envelope mass. The CO abundance drops when going from a pre-stellar core, to a Class 0, to a Class I object. We compare our results to the data presented by Jørgensen et al. (2002) who derived global envelope abundances for 18 sources. Their result is shown in Fig. 10, where open symbols are Class I objects, closed diamonds are Class 0 objects, and the filled squares are pre-stellar cores. Superposed on the data are curves based on our models. To first order our models show the same trend. The observations show no evidence for freeze-out in the Class I objects but the number of this type of source is small and the derived envelope masses and abundances are somewhat uncertain. We also expect some amount of intrinsic scatter due to the unique environments and characteristics of each source. Again the drop abundance model and Model 3 including cosmic rays and a low binding energy show too high CO abundance (or too little depletion). Unfortunately, our simulation begins with only one solar mass and therefore we do not catch the more massive Class 0 and pre-stellar cores.

We can also calculate gas column densities based on our abundance distribution models. Vertically integrated column densities, $N_{CO} = \int n_{CO}(z) dz$, are shown at four different free-fall times in Fig. 11. The models differ mostly on the position of the evaporation front as a result of the different binding energies used. The column density profiles at $t = 0$ can be compared to those presented by Aikawa et al. (2001, 2003, 2005). Although our underlying density model is different, the column densities are comparable, differing by an order of magnitude or less. Aikawa et al. show flat profiles toward the core center

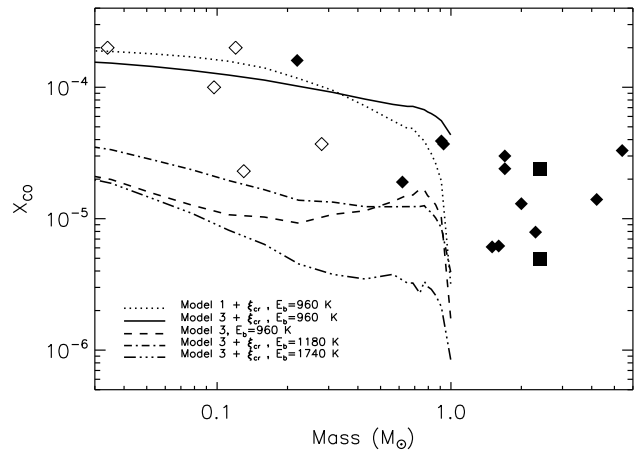


Fig. 10. In this plot we show the abundance as function of envelope mass. Also shown in this plot are data points taken from Jørgensen et al. (2002, 2005). The open symbols are Class I objects, the filled diamonds are Class 0 sources, and the filled squares are pre-stellar cores.

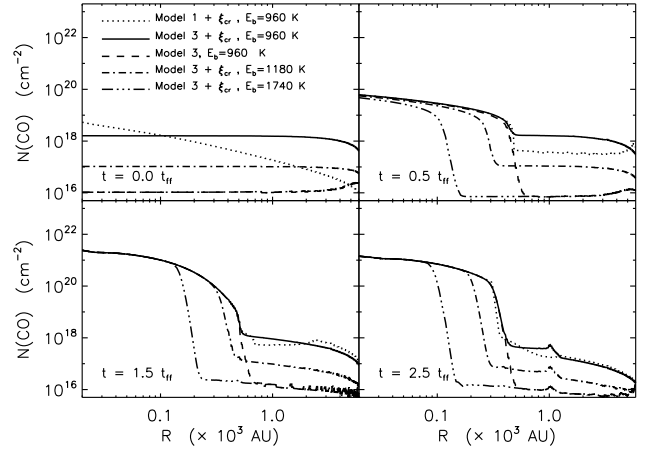


Fig. 11. CO gas column densities of the models discussed in this paper. These profiles are seen through a pencil beam, and need to be convolved with an appropriate beam in order to be directly compared to observations.

or slight drops within ~ 5000 AU, which is the same trend we find with our models. The only exception is our drop abundance model (Model 1) which gives an increasing column density toward the center. The drop occurs at ~ 6000 AU, and within a 6000 AU radius we have a constant abundance. The n_{H_2} density decreases quadratically with radius which means that the column density of CO increases toward the core center. This is in disagreement with observations (e.g., Tafalla et al. 2004) where flat or decreasing integrated intensity profiles are found in core centers, which can be interpreted as a drop in the column density.

Column densities drop around three orders of magnitude from the center toward the freeze-out zone in the disk, comparable to Aikawa et al. (1996), although column densities in our results are generally more than one order of magnitude higher. This is simply explained by the differences in the adopted disk masses. A typical value adopted for disk masses is $10^{-2} M_{\odot}$, while the disk in our simulations grows to an unrealistically high

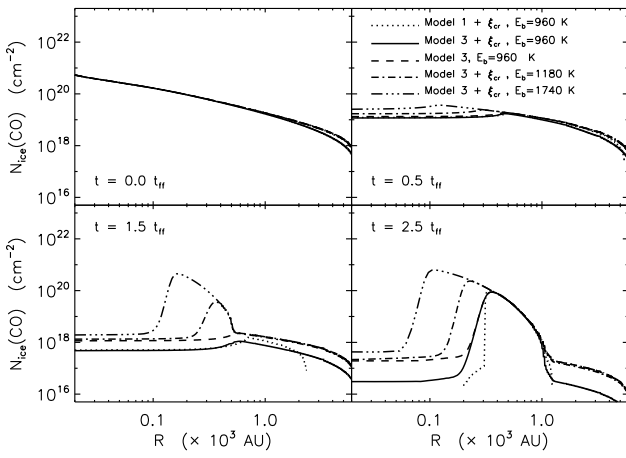


Fig. 12. Same as Fig. 11 but for CO ice column densities.

mass of about $0.4 M_{\odot}$. Also our column density distributions are somewhat more complicated as we do not use a simple analytic description of a non-evolving disk. Aikawa et al. (1996) get drops in column density due to freeze-out in the disk around 200 – 300 AU, similar to our results of 100 – 500 AU, depending on which model we use.

In a similar way we can calculate the column densities for the CO bound to ice. Plots of the ice column densities are shown in Fig. 12. Before collapse the column density of CO ice increase inwards due to the shorter freeze-out timescales there. When the central temperature rises, the column density flattens and drops, while in the protoplanetary disk the column density sharply increases. Overall, the column density drops in the envelope because of the decreasing density (which also results in a lower freeze-out rate). It is difficult to compare these results with observations since often cold (unrelated) clouds, where CO is frozen out, lie in front of protostars. Considering this, observed column densities of CO ice lie often around 10^{18} cm^{-2} in reasonable agreement with our results.

3.6. Emission lines

Simulated spectral lines are a direct way to test our models since these can be compared directly to observed spectra. As mentioned in Section 2, we use the hydrodynamical time snapshots including the abundance distribution mapped onto the original grid as input models for our 2D molecular excitation code *RATRAN*. This code solves the level population using an accelerated Monte Carlo method, which is then ray-traced to make frequency dependent intensity maps. After beam convolution, spectral profiles can be extracted from these and directly compared to observations. We add a mean field of 0.2 km s^{-1} to the snapshots during the radiation transfer calculations to emulate the presence of micro-turbulence.

An in-depth analysis of spectra based on the hydrodynamical simulation is given in a separate paper (Brinch et al. *in prep.*) and only example spectra of the abundance models derived in this paper are presented here. Figure 13 shows the CO $J = 3-2$ transition of the four time snapshots which have been used in the previous figures. The top three panels correspond to the three abundance models including cosmic ray desorption, while the lower three panels show spectra based on model 3 without cosmic ray desorption and with increasing binding energies. Figure 14 has a similar layout, but for the less optically thick isotopologue C^{18}O . For comparison, CO and C^{18}O spectra, cal-

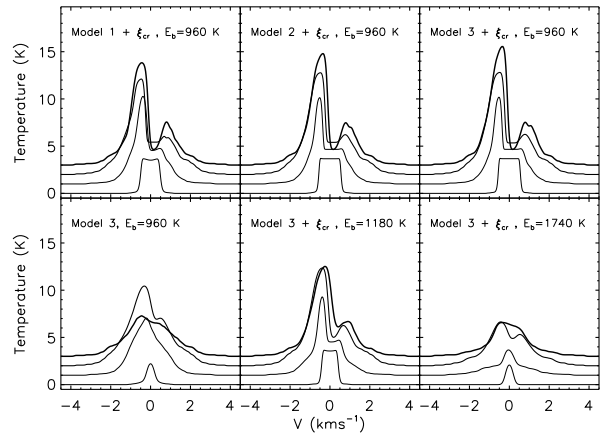


Fig. 13. Time series of CO 3–2 spectra. The top three panels show the three different abundance models. The three lower panels show model 3, including cosmic ray desorption using three different binding energies. Time is shown by increasing line thickness and the four lines correspond to the four adopted time snapshots (0.0, 0.5, 1.5, and 2.5 t_{ff}). Each line has been offset by 0.5 K.

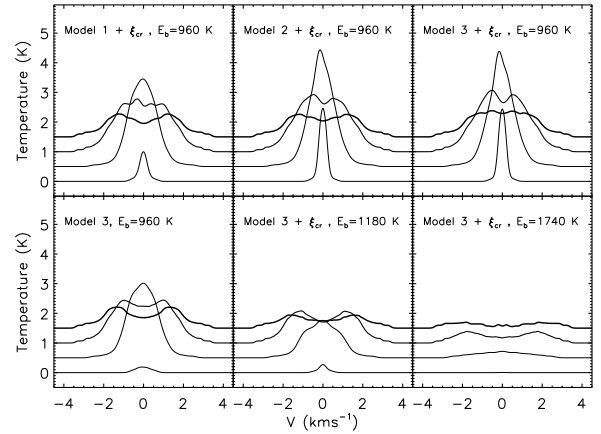


Fig. 14. Similar to Fig. 13 but for C^{18}O 3–2.

culated with a constant abundance profile are shown in Fig. 15. All spectra are seen under a 90° inclination (edge-on; similar to the orientation of the model in Fig. 1), and they have all been convolved with a $10''$ beam which is a typical value for single-dish sub-millimeter telescopes. A distance of 140 pc (Taurus star forming region) is adopted. We use an isotopic $^{16}\text{O}:^{18}\text{O}$ ratio of 560 (Wilson & Rood 1994) to calculate all C^{18}O spectra.

First of all, we see that the spectra in the top row of Fig. 13 are largely similar to each other and also to the constant abundance profiles in Fig. 15. The reason is that CO gets optically thick before the abundance goes down and thus they are independent of the underlying abundance model. Therefore we cannot use CO spectra to distinguish between the three models and we cannot determine the depletion factor using CO. Excluding cosmic rays or increasing the binding energy have the effect on the spectra of lowering the intensity, and in this case CO can be used to constrain the models.

The line profile of the earliest snapshot (the thinnest line) is seen to have a very boxy shape with a flat line center. This is entirely due to the hydrodynamical model, which has not yet

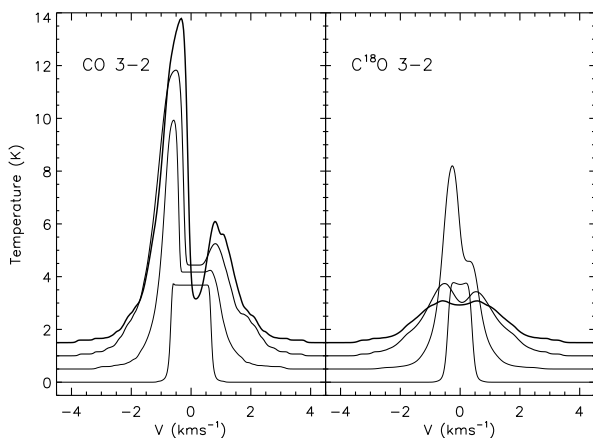


Fig. 15. Time series of CO and C¹⁸O spectra with a constant abundance profile. Time is represented by increasing line thickness.

evolved from its initial isothermal state in the region where the line get optically thick. Basically we probe the same temperature through a range of velocities, which gives rise to the flat top. The line of the earliest snapshot is also considerably more narrow than the other lines. This is because the velocities in the model have not yet had the time to build up.

The C¹⁸O spectra however are seen to differ considerably from the ones calculated from a constant abundance model. They also differ, although somewhat less, from each other when the three abundance models are compared. The reason is that the lines are optically thin and therefore a drop in the abundance has a direct impact on the spectral line, no matter where the drop occurs.

The spectra shown here are all simulating single-dish measurement, where the emission of the source has been smeared out in a relatively large beam. If instead an interferometer is used, beam sizes better than 1'' can be obtained, which allows us to map the line-of-sight column densities. With such observations, it should in principle be possible to map out the abundance distributions of optically thin species and constrain the models.

4. Discussion

The abundance profiles presented here depend on the adopted hydrodynamical model. While we believe that the overall behavior of our results are generally applicable, details such as the exact timescale and the absolute values of the fractional depletion depend on the initial conditions of our simulation such as mass and angular momentum and also on the particular hydrodynamical scheme which we have used.

A main concern regarding the hydrodynamics is the internal radiation transfer module that is used to calculate the temperature structure of the simulation. This is done with an approximate method which is known to overestimate the dust temperature by a few Kelvins compared to calculation done by a more accurate continuum radiation transfer code (Visser, priv. comm.). While a few Kelvin have little or no effect on the hydrodynamics and therefore on the evolution of the cloud, it can certainly make a difference for the evaporation front which has a strong temperature dependence. While this will affect the detailed behavior of the abundances, it will not change the general trends discussed in this paper.

Although in this paper we only concerned ourselves with the CO gas-phase abundance, as mentioned in Sect. 2, our method can be easily extended to include other species and even surface reactions. However, running the full chemical network is considerably more computationally demanding. Whereas the CO model runs in a few hours on a standard desktop computer using 9×10^5 trace particles, a test run of the full chemical network showed that it takes a factor of 100 longer to run using a factor of 1000 less trace particles. Nevertheless, such large scale chemical models present a powerful way to obtain realistic abundance profiles for hydrodynamical simulations which instruments like the Atacama Large Millimeter Array (ALMA) can test at high spatial resolution.

5. Conclusion

In this paper we have investigated different scenarios for the depletion of CO in a collapsing cloud. We have used a hydrodynamical code to describe the dynamical evolution of the cloud and the chemistry has been solved using a trace particle approach.

Of the various models shown in Sect. 3 the one which exclude cosmic ray desorption and the ones using higher binding energies differ the most. The drop abundance model provides a good approximation to Model 2 and 3. Therefore, if it is possible to fit a drop profile to observations, as was done by Jørgensen et al. (2005), it should be possible to run a hydrodynamical simulation with customized initial conditions, so that it reproduces this profile and thereby putting an observational constraint on the hydrodynamics. Also in cases where an analytical model is used, using the drop abundance approximation is quite good.

We furthermore conclude that the freeze-out chemistry has little effect on optically thick spectral lines, especially when observed in low resolution. It is therefore not entirely unreasonable to model such lines using a constant abundance model disregarding the chemistry. However, one should be careful when using optically thin lines to determine which average gas phase abundance to use for a constant abundance model, since the average abundances derived from such lines are indeed depending on the freeze-out chemistry. The maximum discrepancy between the flat abundance profile model (Fig. 15) and the freeze-out models shown in Fig. 14 is a factor of three in the integrated intensity. Such a change in the average abundance does not affect the optically thick lines a lot, so depending on the accuracy needed, using a flat abundance distribution to model data in which freeze-out is present may not be entirely unreasonable.

Finally, the effect of the chemical depletion is considerably enhanced when the resolution of the observations is increased, making it more important to get the abundance profiles right. This will especially be important for future ALMA observations (with a resolution of $\sim 0.01''$) where the level of detail will be so great that getting the exact abundances will be crucial for interpreting the data.

Acknowledgments The authors would like to thank the anonymous referee for thorough and useful comments. CB is partially supported by the European Commission through the FP6 - Marie Curie Early Stage Researcher Training programme. The research of MRH is supported through a VIDI grant from the Netherlands Organization for Scientific Research.

References

- Adams, F. C., Lada, C. J., & Shu, F. H. 1987, ApJ, 312, 788
- Aikawa, Y., Herbst, E., Roberts, H., & Caselli, P. 2005, ApJ, 620, 330
- Aikawa, Y., Miyama, S. M., Nakano, T., & Umebayashi, T. 1996, ApJ, 467, 684
- Aikawa, Y., Ohashi, N., & Herbst, E. 2003, ApJ, 593, 906
- Aikawa, Y., Ohashi, N., Inutsuka, S.-i., Herbst, E., & Takakuwa, S. 2001, ApJ, 552, 639
- Bacmann, A., Lefloch, B., Ceccarelli, C., et al. 2002, A&A, 389, L6
- Bergin, E. A., Alves, J., Huard, T., & Lada, C. J. 2002, ApJ, 570, L101
- Brinch, C., Crapsi, A., Hogerheijde, M. R., & Jørgensen, J. K. 2007, A&A, 461, 1037
- Caselli, P., Walmsley, C. M., Tafalla, M., Dore, L., & Myers, P. C. 1999, ApJ, 523, L165
- Charnley, S. B., Rodgers, S. D., & Ehrenfreund, P. 2001, A&A, 378, 1024
- Collings, M. P., Anderson, M. A., Chen, R., et al. 2004, MNRAS, 354, 1133
- Crapsi, A., Caselli, P., Walmsley, C. M., et al. 2004, A&A, 420, 957
- Draine, B. T. & Lee, H. M. 1984, ApJ, 285, 89
- Evans, II, N. J. 1999, ARA&A, 37, 311
- Fraser, H. J., Collings, M. P., Dever, J. W., & McCoustra, M. R. S. 2004, MNRAS, 353, 59
- Hasegawa, T. I. & Herbst, E. 1993, MNRAS, 261, 83
- Hasegawa, T. I., Herbst, E., & Leung, C. M. 1992, ApJS, 82, 167
- Hogerheijde, M. R. & van der Tak, F. F. S. 2000, A&A, 362, 697
- Jessop, N. E. & Ward-Thompson, D. 2001, MNRAS, 323, 1025
- Jørgensen, J. K., Schöier, F. L., & van Dishoeck, E. F. 2002, A&A, 389, 908
- Jørgensen, J. K., Schöier, F. L., & van Dishoeck, E. F. 2005, A&A, 435, 177
- Lada, C. J. & Wilking, B. A. 1984, ApJ, 287, 610
- Lee, J.-E., Bergin, E. A., & Evans, II, N. J. 2004, ApJ, 617, 360
- Shakura, N. I. & Sunyaev, R. A. 1973, A&A, 24, 337
- Shen, C. J., Greenberg, J. M., Schutte, W. A., & van Dishoeck, E. F. 2004, A&A, 415, 203
- Tafalla, M., Myers, P. C., Caselli, P., & Walmsley, C. M. 2004, A&A, 416, 191
- Tsamis, Y. G., Rawlings, J. M. C., Yates, J. A., & Viti, S. 2008, ArXiv e-prints, 803
- van Weeren, R. J. 2007, Master's thesis, Leiden University
- Watson, W. D. & Salpeter, E. E. 1972, ApJ, 175, 659
- Wilson, T. L. & Rood, R. 1994, ARA&A, 32, 191
- Woodall, J., Agúndez, M., Markwick-Kemper, A. J., & Millar, T. J. 2007, A&A, 466, 1197
- Yorke, H. W. & Bodenheimer, P. 1999, ApJ, 525, 330